

Galactic Observations at 31, 42 and 144 GHz with the Mobile Anisotropy Telescope

J. L. Puchalla¹, R. Caldwell², K. L. Cruz¹, M. J. Devlin¹, W. B. Dorwart², T. Herbig²,
A. D. Miller², M. R. Nolta², L. A. Page², E. Torbet², H. T. Tran²

ABSTRACT

We present multi-frequency maps of a portion of the Galactic Plane centered on a declination of -60° with resolutions ranging from $0^\circ.2$ to $0^\circ.9$. The maps are optimized to detect unresolved source emission and are cross-calibrated against the planet Jupiter. We discuss six millimeter-bright regions, three of which are visible in all bands, and list measured flux densities. Variability is limited to less than 3.8% for all sources seen at 31 and 42 GHz and less than 10% at 144 GHz. Fractional polarization limits smaller than 0.08 are measured for all sources seen at 31 and 42 GHz. No fractional polarization limits are reported at 144 GHz.

Subject headings: Galaxy: structure — (ISM:) HII regions — radio continuum: general — surveys

1. Introduction

Galactic radiation at centimeter and millimeter wavelengths is attributed to a combination of the following sources of emission: synchrotron, free-free, thermal interstellar dust and variations in the electric and magnetic dipoles of dust (*i.e.* spinning dust). Large-area, multi-frequency surveys help us to understand the objects and environments which emit in the far-infrared and assist in determining the mechanisms driving microwave emission. The atmosphere is relatively opaque at these frequencies making such surveys difficult to perform from low altitudes. At present, the only comprehensive microwave survey data available is from the Cosmic Background Explorer (*COBE*) (Bennett *et al.* 1996). It will not be until the launch of the Microwave Anisotropy Probe (*MAP*) satellite in late 2000 that a full sky survey with pixel resolution smaller than 1° will be completed.

Bright millimeter-wavelength sources are important for cosmology as calibrators and a possible Cosmic Microwave Background (CMB) foreground contaminate (Toffolatti *et al.* 1999; Sokasian *et al.* 1998).

¹University of Pennsylvania, Department of Physics and Astronomy, David Rittenhouse Laboratory, Philadelphia, PA 19104 e-mail contact: puchalla@higgs.hep.upenn.edu

²Princeton University, Physics Department, Jadwin Hall, Princeton, NJ 08544

There are several open questions about this class of object that include: what are their spectra; are they variable; are they polarized? We address these questions for six Galactic sources using observations made with the Mobile Anisotropy Telescope (*MAT*). We focus on characterizing emission from unresolved and localized millimeter-bright regions. These data will also help assess daytime atmospheric conditions relevant to observations from similar Chilean sites. We present maps of the Galactic Plane centered on a declination of -60° (approximately $280^\circ < l < 305^\circ$ and $-8^\circ < b < 4^\circ$) covering several bright regions including the Carinae Nebula and RCW 57.

All of the millimeter-bright objects we observe have *IRAS* counterparts or are known *HII* regions. The *IRAS* survey indicates that most of these contain substructure unresolved by the *MAT* observations. Since they cannot be uniquely labeled with previous surveys we denote each bright region with number from 1 to 6. Figure 1 shows the region covered by these observations. Table 1 lists some of the known radio and millimeter-bright sources observed in other surveys which comprise these regions. The list of associated names gives the brightest far-infrared and radio sources in the vicinity.

2. Instrument and Observations

MAT is a 0.8 m diameter aperture telescope based on the design in Wollack *et al.* (1997). Three frequency bands (31, 42, 144 GHz) in eight channels are monitored. The telescope is steerable in azimuth but fixed in elevation. The focal plane contains five corrugated feeds. Observations are made in two polarizations in Ka-band (26-36 GHz) and Q-band (36-46 GHz) using total power high electron mobility transistors (HEMT) amplifiers. Observations are also made in D-band with two single polarization SIS receivers with dual sidebands (≈ 138 -140 GHz and ≈ 148 -150 GHz with the local oscillator center at 144 GHz). The calibration and antenna patterns are measured in the field using multiple observations of Jupiter ($\theta_{disk} \approx 30''$ -45''). Table 2 lists the *MAT* beam characteristics for each frequency. Antenna patterns are modeled as two-dimensional Gaussian profiles parameterized by an amplitude and two orthogonal widths³ σ_H and σ_V . The H and V denote the horizontal (chop direction) and vertical (meridian) line with respect to the local horizon. Except for one of the SIS channels (D2) not located in the center of the focal plane, all antenna patterns are well approximated by Gaussian profiles.

The center of the focal plane is fixed at an elevation of $40^\circ.76$. A flat mirror sweeps the beams with an amplitude of 3° on the sky in a sinusoidal pattern at 3.7 Hz. When the mirror is set to zero amplitude, the center of the focal plane is at an azimuth of $207^\circ.41$ East of North. Each day, *MAT* views a band about the South Celestial Pole of constant mean declination. To view calibrators and other bright objects, the telescope base is slewed to a new azimuth and the source drifts through the field of view. This procedure typically requires 20 minutes.

³FWHM is related to σ by $\sigma = \Theta_{FWHM}/[2(2\ln 2)]^{\frac{1}{2}}$.

Table 1: Location of each of the *MAT* regions along with known radio and infrared-bright objects contained therein. The approximate location of the centroid is listed to a precision appropriate for all *MAT* frequencies. MAT 5 and MAT 6 are sub-categorized for the 144 GHz channels since multiple sources are resolved. IRAS-PSC denotes the *IRAS* point source catalog.

MAT Object	Center RA	Center Dec	Associated Names	Type
MAT 1	151°.8	−57°.3	IRAS 10049-5657	IRAS-PSC
			RCW46	HII region
MAT 2	156°.0	−57°.8	RCW49	HII Region
			NGC 3247	Open Cluster
MAT 3	161°.0	−59°.7	η Carinae	Nebula
			IRAS 10414-5919	
MAT 4	165°.1	−61°.1	IRAS 10591-6040	IRAS-PSC
			IRAS 10589-6034	
MAT 5	168°.6	−61°.3	RCW57	HII Region
MAT 5a	167°.90	−61°.35	NGC 3576	HII Region
MAT 5b	168°.7	−61°.30	NGC 3603	OB Cluster
MAT 5b				HII Region
MAT 6	183°.3	−62°.9		IRAS-PSC
MAT 6a	182°.48	−62°.82	IRAS 12073-6233	
MAT 6b	183°.84	−63°.00	IRAS 12127-6244	

Table 2: *MAT* beam characteristics. The D2 beam response is not well modeled as a Gaussian below -10dB.

Center Freq. (GHz)	Channel	σ_H (deg)	σ_V (deg)	Solid Angle ($\Omega \times 10^{-5}$ str)
31	Ka1&2	0.39	0.39	30
42	Q1&Q2	0.28	0.28	15
42	Q3&Q4	0.31	0.29	18
144	D1	0.086	0.082	1.4
144	D2	0.13	0.12	2.9

Observations were carried out at 5200 m from Cerro Toco⁴ at latitude 22°95 S, longitude 67°78 W. For this paper we present data obtained between August 30, 1998 and October 14, 1998. The primary goal of the experiment was to use nightly observations far from the Galactic Plane ($b > 15^\circ$) to measure the anisotropy in the CMB radiation (Miller *et al.* 1999; Torbet *et al.* 1999; Dodelson *et al.* 1999). This observation scheme also provides a daily view of a large section of the Galactic Plane.

2.1. Calibration

Jupiter’s emission spectrum is complicated by several molecular lines. However, for wideband observations such as those made by *MAT*, Jupiter is stable and its intrinsic brightness temperature has been measured to $\approx 5\%$ (Ulich *et al.* 1981; Griffin *et al.* 1986; Goldin *et al.* 1997). We use the values 152 K, 160 K, and 170 K for the 31, 42 and 144 GHz bands respectively.

Four terms contribute most to the uncertainty of the calibration of each channel: (1) the standard deviation in the measured solid angle; (2) the standard deviation in the measured temperature of Jupiter for each channel; (3) the intrinsic uncertainty of the brightness temperature of Jupiter; (4) the uncertainty due to calibration drift between Jupiter observations. For the SIS channel used in this analysis, the first three terms contribute uncertainties of 5.5%, 7%, and 5%, respectively. For the HEMT channels, the corresponding values are less than 7%, 10%, and 5%. These terms add in quadrature. The fourth term is primarily the result of diurnal temperature variations.

To monitor calibration changes between observations of Jupiter, the HEMT-based channels are injected with a signal from a thermally-stabilized noise source for 40 ms twice every 100 seconds. The SIS-based channels are coupled to a 149 GHz tone at an effective temperature of ~ 1 K. These data indicate a 5% random uncertainty in both the SIS and HEMT calibrations and a $< 2.5\%$ gain change at the time of the Galactic observations. After accounting for the gain change, we estimate the total calibration uncertainty for each channel by adding the uncorrelated errors in quadrature giving a 11% error for the SIS channel and a 14% error for the HEMT channels. The uncertainty quoted in Miller *et al.* is smaller than that stated here because there was little temperature change, and consequently little gain drift, between the Jupiter observations and the CMB observations.

2.2. Pointing

Pointing is established through both rising and setting observations of Jupiter. A nominal central azimuth and beam elevation are assumed initially. A Global Positioning System (GPS) time-stamp is stored with each data point and is used to fix the time and location of the centroid of

⁴The Cerro Toco site of the Universidad Católica de Chile was made available through the generosity of Prof. Hernán Quintana, Dept. of Astronomy and Astrophysics. It is near the proposed MMA site.

the measured antenna pattern for each horn. Ephemeris data are then used to calculate a position error. The nominal central azimuth and beam elevation⁵ are then adjusted to minimize the variance between the expected and predicted location of Jupiter.

This model allows an accurate reconstruction of pointing over the full azimuthal range of the telescope for the data considered here. After coadding the data for this analysis, the effective center of each of the 5 horns’ antenna patterns is determined with an absolute accuracy of $0^\circ.045$ and a relative accuracy of $< 0^\circ.01$ degrees.

3. Data Reduction

We consider a subset of daily observations of the Galactic Plane that contains several millimeter-bright sources. Each of the 8 amplifier channels is processed independently. We do not include the 144 GHz channel D2 since its larger beam greatly decreases its sensitivity to unresolved sources.

Of the total collected Galactic data, 54% are rejected due to signal saturation in one or more channels and $< 1\%$ are rejected based on telemetry drop-outs and noise-injector operation; this procedure leaves approximately 15 observations of 2.68 hours each.

Data are coadded for each chopper cycle based on the position of the chopping mirror. The chopper position over a cycle never deviates from the average cycle for the entire observation region by more than 1%. The 144 GHz channels are binned into samples of $0^\circ.045$ in azimuth for 40 chopper cycles (about 11 seconds). The Ka and Q channels are binned into samples three times larger. By fixing the number of chopper cycles coadded and knowing both the time associated with each data point and the location of each horn antenna pattern (from previous observations of Jupiter), we construct an unfiltered map of the sky.

The quality of daytime observations at this time of year is degraded from those at night. This effect is well correlated to the rise in local temperature above 0°C . We remove the contribution from atmospheric emission to these Galactic observations using a purely spatial filter. After performing a 10σ cut on isolated points (i.e. inconsistent with the point spread function) we remove a slowly varying polynomial from each coadded azimuthal strip. In this technique, a sliding box-car average is generated. Points greater than 2.5σ as well as the four nearest neighbors are flagged. The sliding box-car average is then regenerated with the flagged points removed from consideration. The results are insensitive to small changes in this flagging level. In all channels, the box-car is 2 times the size of the FWHM of the antenna pattern for that channel. This second average is subtracted from the unfiltered data.

Monte Carlo analysis on simulated maps constructed from measured atmospheric data at this site show that this filter effects measurements of the amplitude and width of a Gaussian beam by

⁵Measurements of Galactic sources indicated a tilt in the base of the telescope of $0^\circ.10$.

$< 1\%$ for the atmospheric conditions encountered in this data set. The largest adverse effects occur at the edge of the maps where incomplete coverage of a source can be confused for an atmospheric variation. This occurs with two sources for one feed horn (Q3&4) and, hence, the measured source amplitudes for these channels have been omitted from all averages.

4. Maps

After filtering, each daily map is coadded with observations from other days to produce final images of the region. Each map is comprised of between 10 and 15 coadded viewings. No attempt has been made to coadd maps made from different amplifier channels. We show representative plots of the Galactic region at 31, 42 and 144 GHz in Figure 2, 3, and 4 respectively. Also shown are close-ups of each source region for the frequencies at which they were observed.

Each source close-up is comprised of color contours and an intensity color-bar associated with the *MAT* data. *IRAS*⁶ intensity contours have also been superimposed to demonstrate relative pointing and additional bright sources in the region not seen at all of the *MAT* frequencies.

We are able to place constraints on both polarization and variability of those sources observed at 31 and 42 GHz. Though all detector channels are polarized, the antenna response of orthogonal polarizations in Ka and Q bands are matched. This allows the fractional polarization $2(E_{||} - E_{\perp})/(E_{||} + E_{\perp})$ over the source to be constrained as well as test for systematic errors. Table 3 gives the measured fractional polarization limits for each source over a 3σ region. All sources are unpolarized to the level of our sensitivity.

Nearly all compact radio sources demonstrate some variability on times scales ranging from a few days to years. The variability in emission for the *MAT* sources is constrained over the observing period in all frequency bands. We place limits on the daily and total variation of peak brightness temperatures for all sources observed at 31 and 42 GHz except MAT 4. Due to the lower signal-to-noise of MAT 4 and all sources at 144 GHz we group these observations into 3 subsets in time; the limits are only on the total variation. Daily variation is defined as the standard deviation of all observations about a line. Total variation is the standard deviation on the mean value of all observations. Table 4 shows the limits to which all sources are stable over the observing period. No statistically significant change in brightness is indicated over any time frame.

5. *MAT* Sources: Discussion

The six *MAT* sources are extended at $100\mu\text{m}$ in the *IRAS* maps and cannot be unambiguously resolved in any of the *MAT* beams. For this reason, the flux density from each identified bright

⁶Released data product at <http://www.ipac.caltech.edu/>

Table 3: Fractional polarization limits at 31 and 42 GHz. Due to location, MAT 1 and MAT 2 are only observed by the 42 GHz channels.

MAT Object	Freq. (GHz)	Frac. Polarization Limit
MAT 1	42	< 0.06
MAT 2	42	< 0.05
MAT 3	31	< 0.02
	42	< 0.01
MAT 4	31	< 0.03
	42	< 0.03
MAT 5	31	< 0.03
	42	< 0.04
MAT 6	31	< 0.02
	42	< 0.08

Table 4: Limits on (D) daily and (T) total brightness temperature variation. N.A. indicates that placing this limit is not possible from these data.

MAT Object	Freq. (GHz)	1σ Limit on (D) Daily Variability	1σ Limit on (T) Total Variability
MAT 1	42	D<13.4%	T<3.8%
MAT 2	42	D<5.4%	T<1.5%
MAT 3	31	D<1.6%	T<0.5%
	42	D<3.0%	T<0.8%
	144	N.A.	T<8.5%
MAT 4	31	N.A.	T<7.5%
	42	D<5.5%	T<1.5%
MAT 5	31	D<4.3%	T<1.2%
	42	D<7.2%	T<2.0%
a	144	N.A.	T<8.6%
	b	144	N.A.
MAT 6	31	D<4.6%	T<1.3%
	42	D<8.5%	T<2.4%
a	144	N.A.	T<10%
	b	144	N.A.

region is determined within a circle whose radius is the average 1σ and 2σ beam width for that frequency. That is, the flux density at frequency ν is:

$$S_\nu = \int_{n\sigma} \frac{2kT(x,y)\nu^2}{c^2 10^{-26}} dx dy \quad \text{Jy} \quad (1)$$

where $n\sigma$ denotes the area (number of σ) over which to integrate and $T(x,y)$ is the measured temperature profile over this region. We also quote the amplitude (*i.e.* peak brightness temperature) of the best-fit Gaussian profile (widths unconstrained) for each source. Table 5 details these results.

We average the measurements from all channels of a given frequency. The results at 42 GHz are rescaled to a single beam size of $\Omega_{42GHz} = 16.5 \times 10^{-5} \text{str}$ before averaging. Due to the low signal-to-noise, Q2 is not included in the 42 GHz average.

The quoted uncertainty results from the quadrature sum of the uncorrelated components of the error divided by the number of channels coadded. In addition to calibration error, the sum includes an uncertainty in the baseline of the filtered maps of 4% for the SIS channel and 3% for the HEMT channels.

MAT 1 is an extended HII region containing a single $100\mu\text{m}$ -bright *IRAS* point source. MAT 2 is a compact HII region. Since they are observed only at 42 GHz we cannot constrain the spectral indices. MAT 4 is also an extended HII region containing two moderately bright $100\mu\text{m}$ -bright *IRAS* point sources. It is seen at 31 and 42 GHz but is not measurable at 144 GHz. The implied spectral index based on the low frequency observations is $\alpha = -0.72$ where $S \sim \nu^\alpha$. In this frequency range, the emission is dominated by synchrotron radiation.

MAT 3 is dominated by emission from the Keyhole Nebula. This region contains the known millimeter-bright and variable remnant η Carinae. Cox *et al.* (1995) have stated that at wavelengths greater than 1 cm, η Carinae is dominated by free-free emission but that between 1 cm and 1 mm the spectral index rises to ~ 1 . Cox *et al.* also give evidence of time variability in a one year period of 30%. Since our beam size at 144 GHz is significantly larger, we are not able to constrain the emission of η Carinae but rather the emission from the larger Keyhole Nebula in which it is contained. This region also contains a second source (IRAS 10414-5919) known to be bright at both 4.8 GHz (Condon *et al.* 1995) and $100\mu\text{m}$. Therefore, there is no reason to expect that our map would be centered on η Carinae. Given the extended emission of this region we have not attempted to constrain the spectral index.

MAT 5 and MAT 6 both contain two *IRAS*-bright sources which are clearly seen at 144 GHz. However, the 31 and 42 GHz observations indicate that only one source dominates emission at lower frequencies implying a highly inverted spectrum. For MAT 6a, if we use the flux limit at 42 GHz in conjunction with the measured flux at 144 GHz assuming it is an unresolved source we find a spectral index of $\alpha \geq 1.5$ where $S \sim \nu^\alpha$. For MAT 5a, we find $\alpha \geq 2.0$. Both are consistent with the classical spectra of compact HII regions where $S \sim \nu^2$.

Table 5: Peak brightness temperature and flux density S_ν within a circle of 1σ and 2σ beam widths for the *MAT* sources. No entry for a channel implies the source is not seen or is below the measurable flux density limit of the map. We report the average measured values for each frequency independent of polarization. Quoted errors do not include the 5% intrinsic uncertainty in the brightness temperature of Jupiter. The map limit is the flux density at which an unresolved source would be measured with a signal-to-noise of one.

MAT Object	Freq. Band (GHz)	Peak Temp (mK)	1σ - S_ν (Jy)	2σ - S_ν (Jy)	Map Limit (Jy)
MAT 1					
	42	7.2 ± 0.7	22.2 ± 2.1	60.0 ± 5.7	5.2
MAT 2					
	42	26.6 ± 2.5	85.0 ± 8.1	240.1 ± 22.8	5.2
MAT 3					
	31	65.0 ± 6.2	220.1 ± 20.9	539.2 ± 51.2	7.1
	42	46.3 ± 3.6	178.1 ± 13.9	496.9 ± 38.8	5.2
	144	$8.8 \pm .9$	33.1 ± 3.7	110.6 ± 11.9	12.8
MAT 4					
	31	12.0 ± 1.1	34.1 ± 3.2	83.1 ± 7.9	7.1
	42	7.6 ± 0.7	25.5 ± 2.4	67.6 ± 6.4	5.2
MAT 5					
	31	40.7 ± 3.9	140.8 ± 13.4	341.6 ± 32.5	7.1
	42	28.7 ± 2.2	101.5 ± 7.9	244.9 ± 19.1	5.2
a	144	8.8 ± 0.9	30.6 ± 3.4	67.1 ± 7.3	12.7
b	144	12.4 ± 1.37	46.4 ± 5.1	117.8 ± 12.7	12.7
MAT 6					
	31	17.4 ± 1.7	62.3 ± 5.9	165.5 ± 15.7	7.1
	42	8.8 ± 1.7	24.8 ± 4.6	49.4 ± 9.4	5.2
a	144	3.1 ± 0.7	10.9 ± 2.6	34.2 ± 8.5	12.7
b	144	2.5 ± 0.7	10.2 ± 2.6	28.9 ± 7.2	12.7

We would like to thank Suzanne Staggs, Dave Rusin, Simon Dicker, Jeff Klein, and Neill Reid for helpful conversations and assistance in preparing this manuscript. This work was supported by an NSF NYI award, a Cottrell Award from the Research Corporation, a David and Lucile Packard Fellowship (to LP), a NASA GSRP fellowship to AM, an NSF graduate fellowship to MN, a NSF Career award (AST-9732960, to MD), NSF grants PHY-9222952, PHY-9600015, AST-9732960, and the University of Pennsylvania. The data will be made public upon publication of this article.

REFERENCES

- Bennett, C. L. , Banday, A.J., Gorski, K.M., Hinshaw, G., Jackson,P., Keegstra, P., Kogut, A., Smoot, G.F., Wilkinson, D.T. & Wright, E.L. 1996 ApJ , 464, L1
- Condon, J.J., Griffith, M.R. & Wright, A.E. 1993, AJ, 106, 1095
- Cox, P., Mezger, P.G., Sievers, A., Najarro, F., Bronfman, L., Kreysa, E. & Haslam, G. 1995 Astron. ans Astro., 297:168-174
- Dodelson, S. & Knox, L. 1999, preprint (astro-ph/9909454)
- Goldin, A., Kowitt, M., Cheng, E., Cottingham, D., Fixsen, D., Inman, C., Meyer, S., Puchalla, J., Ruhl, J. & Silverberg, R. 1997, ApJ, 488
- Griffin, M. J., Ade, A. R., Orton, G. S., Robson, E. I., Gear, W.K., Nolt, I. G. & Radostitz, J. V., 1986, *Icarus*, 65, 244
- Leisawitz, D. 1996, AIP Conf. Proc., 348, 287
- Miller, A. D, Caldwell, R., Devlin, M. J., Dorwart, W. Herbig, T., Nolta, Miller, A. D., Page, L., Puchalla, J.L. & Tran, H. 1999, ApJ, in press, (astro-ph/9906421)
- Sokasian, A., Gawiser, E. & Smoot, G. 1998, ApJ, submitted, (astro-ph/9811311)
- Toffolatti, L., De Zotti, G., Argueso, F. & Burigana, C. 1999, preprint (astro-ph/9902343)
- Torbet, E., Devlin, M. J., Dorwart, W. Herbig, T., Nolta, Miller, A. D., Page, L., Puchalla, J.L. & Tran, H. 1999, ApJ, 521, L79
- Ulich, B. L., 1981, *Astr. J.*, 86:11, 1619.
- Wollack, E. J., Devlin, M. J., Jarosik, N.J., Netterfield, C. B., Page, L. & Wilkinson, D. 1997, ApJ, 476:440-447

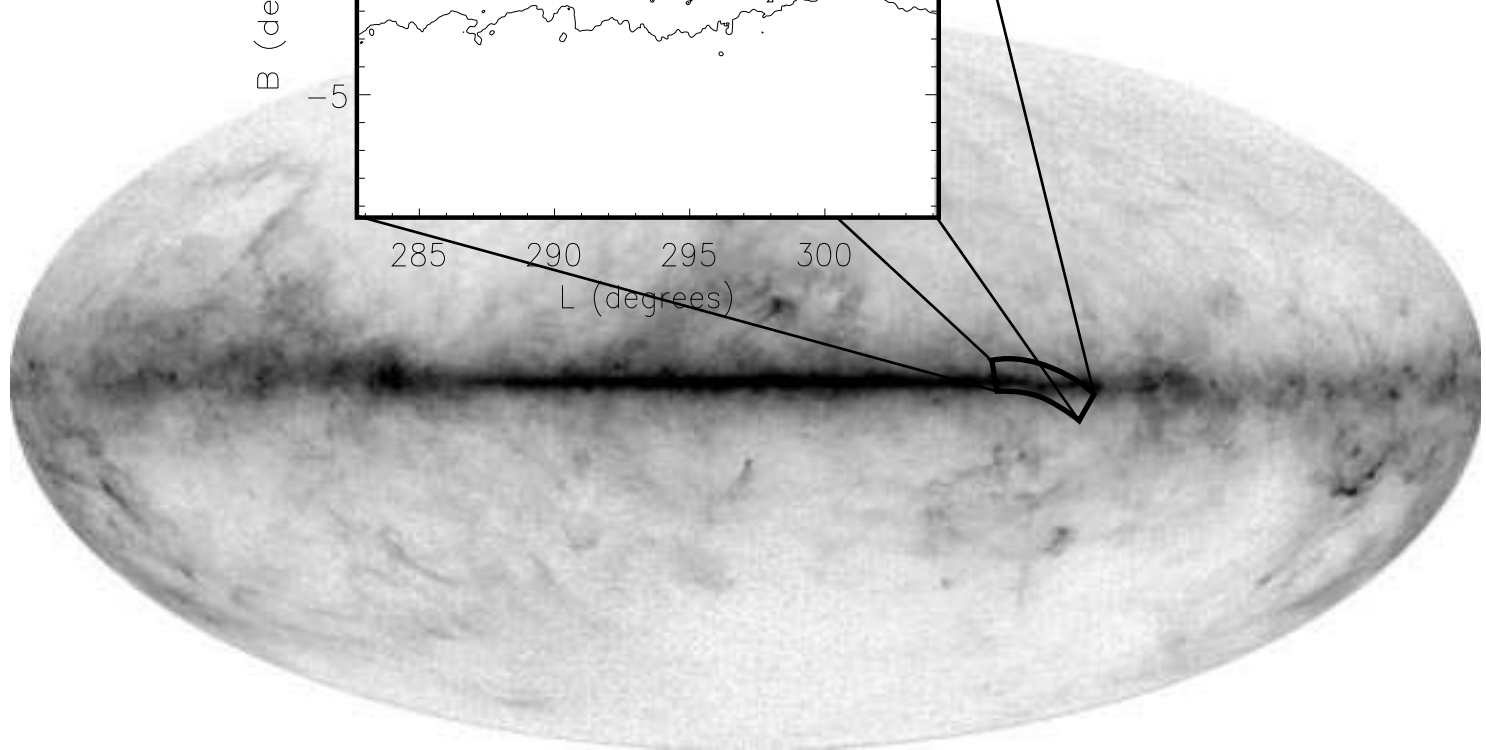
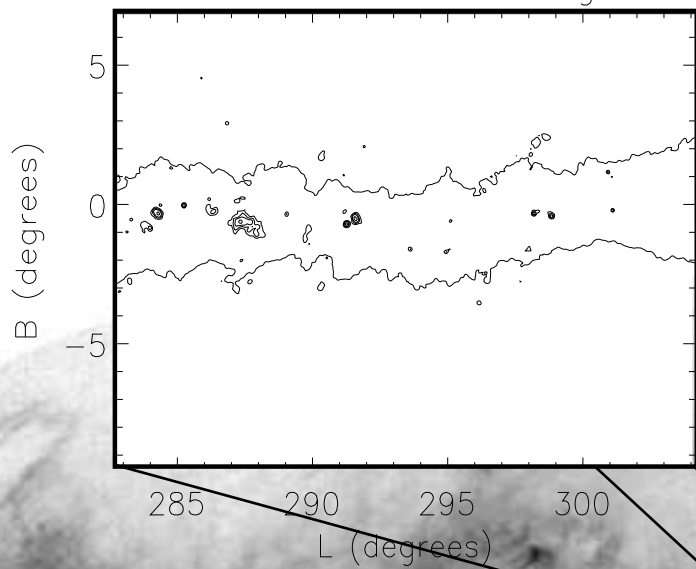
Fig. 1.— The location of the *MAT* observations reported herein superimposed on the DIRBE $240\mu\text{m}$ full sky map (Leisawitz 1996). The inset details this region showing $100\mu\text{m}$ bright contours as seen by *IRAS*.

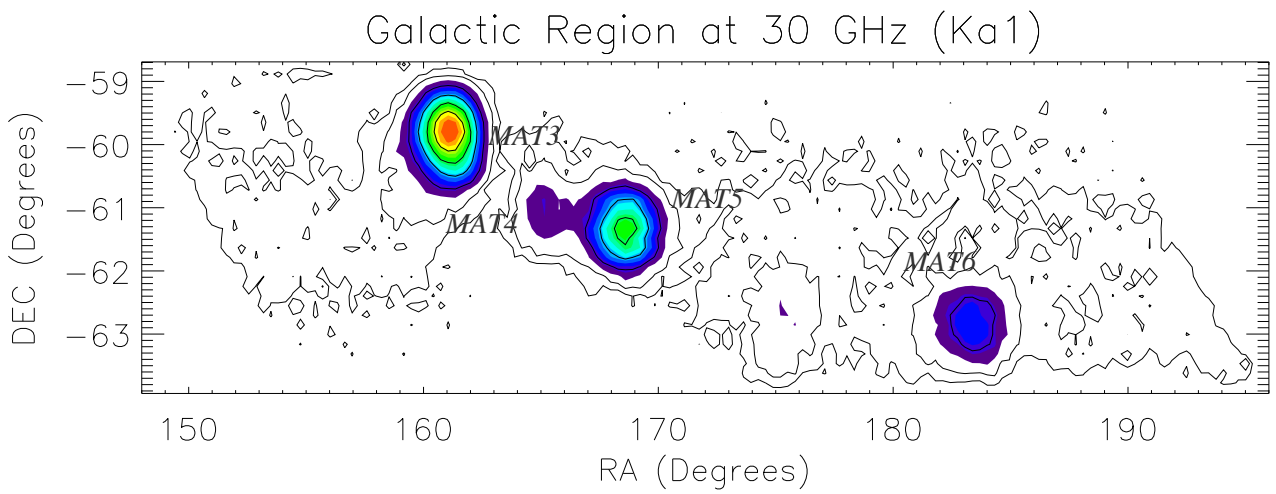
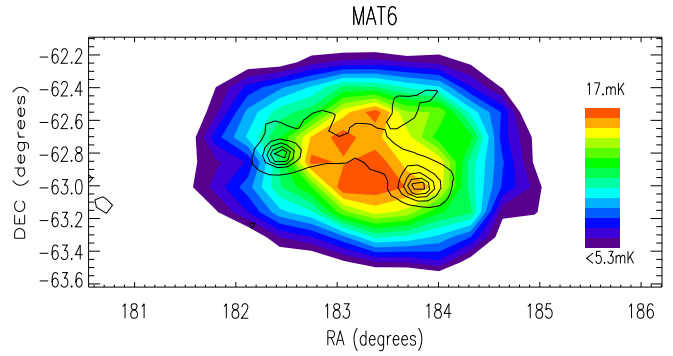
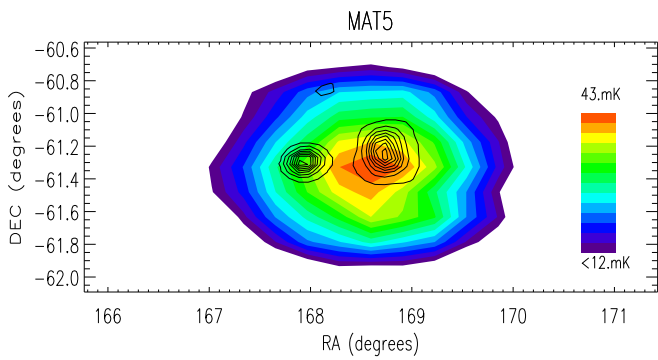
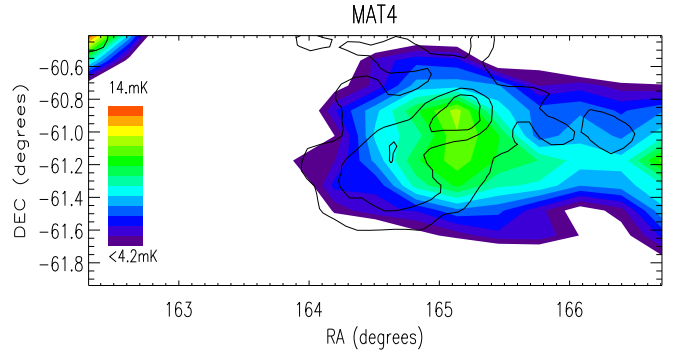
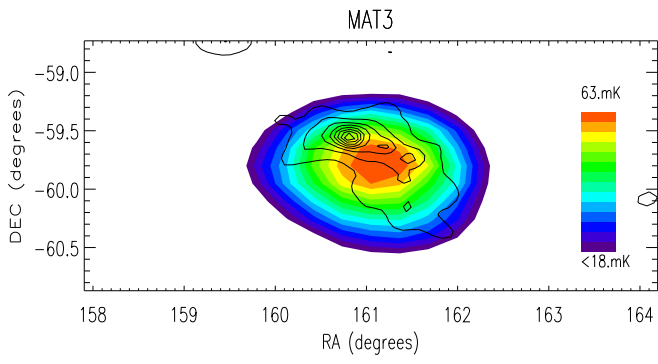
Fig. 2.— Observed sources at 31 GHz with *IRAS* contours and full Galactic region map measured by Ka1. The contours in the lower map are from the *MAT* data.

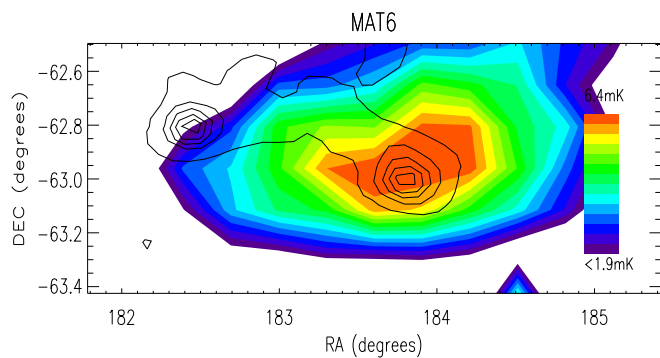
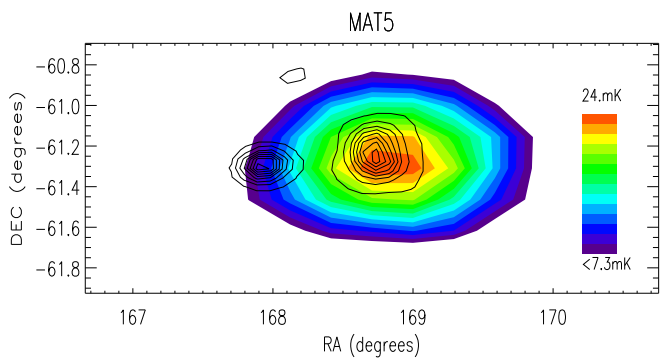
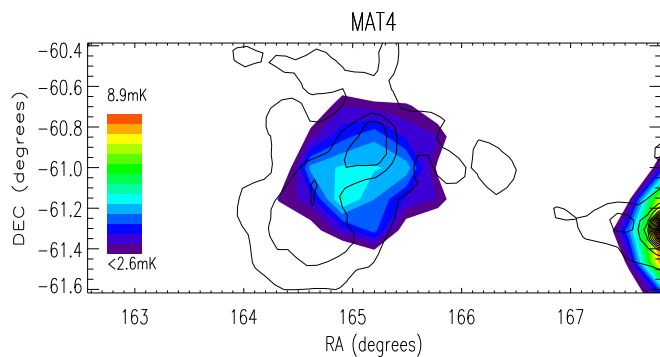
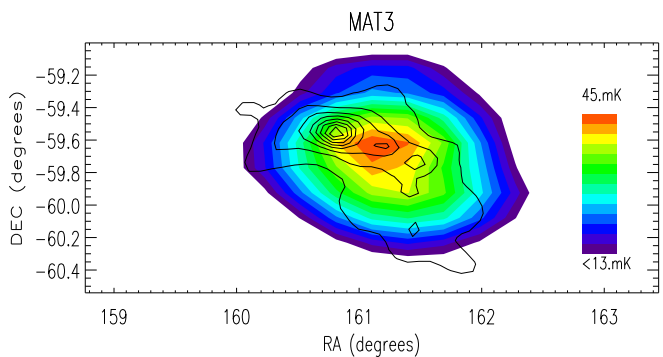
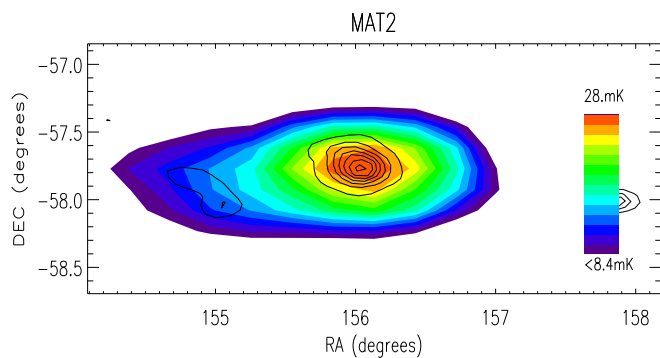
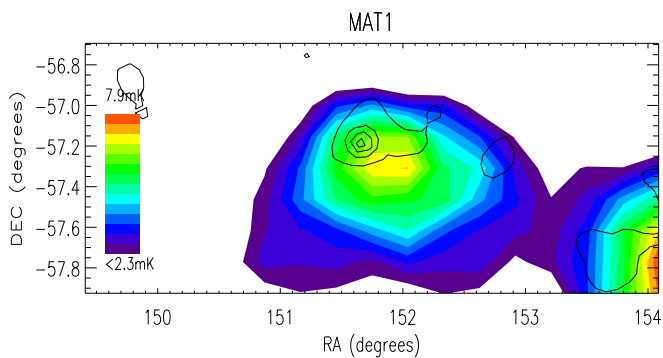
Fig. 3.— Observed sources at 42 GHz with *IRAS* contours and full Galactic region map measured by Q1. MAT6 is not observed by this channel. The contours in the lower map are from the *MAT* data.

Fig. 4.— Observed sources at 144 GHz with *IRAS* contours and full Galactic region map measured by D1. MAT1 and MAT2 is out of the field of view of D1. MAT4 is below the D1 sensitivity limit. The contours in the lower map are from the *MAT* data.

IRAS Detail of MAT Region







Galactic Region at 40 GHz (Q1)

